

# Outstanding Piezoelectricity of (K, Na)(Nb, Sb)O<sub>3</sub>-SrZrO<sub>3</sub>-(Bi, Ag)ZrO<sub>3</sub> Piezoceramics and Their Application to a Planar-Type Actuator

**Su-Hwan Go**

Korea University

**Jae-min Eum**

Korea University

**Dae-Su Kim**

Korea University

**Seok-Jun Chae**

Korea University

**Sun-Woo Kim**

Korea University

**Eun-Ji Kim**

Korea University

**Yeon-Gyeong Chae**

Korea University

**Jong-Un Woo**

Korea University

**S. Nahm** (✉ [snahm@korea.ac.kr](mailto:snahm@korea.ac.kr))

Korea University

---

## Research Article

**Keywords:** KNN-based ceramics, Lead-free piezoceramics, domain structure, crystal structure

**Posted Date:** August 26th, 2021

**DOI:** <https://doi.org/10.21203/rs.3.rs-839903/v1>

**License:** © ⓘ This work is licensed under a Creative Commons Attribution 4.0 International License. [Read Full License](#)

---

# Abstract

Fe<sub>2</sub>O<sub>3</sub>-added 0.96(K<sub>0.5</sub>Na<sub>0.5</sub>)(Nb<sub>0.94</sub>Sb<sub>0.06</sub>)-0.01SrZrO<sub>3</sub>-0.03(BiAg)ZrO<sub>3</sub> [KNNS-0.01SZ-0.03BAZ] piezoceramic was well densified at 1090 °C. It exhibited a large piezoelectric charge constant ( $d_{33}$ ) of 650 pC/N, which is similar to the largest  $d_{33}$  value reported in the literature. This sample has a tetragonal-orthorhombic-rhombohedral (T-O-R) structure, in which each structure has a similar proportion. Moreover, nanodomains (2 nm × 15 nm) with low domain boundary energy were found in this sample, which exhibited relaxor properties. Therefore, the presence of a T-O-R multi-structure and nanodomains is responsible for the large  $d_{33}$  value of this sample. A KNNS-0.01SZ-0.03BAZ thick film was synthesized, and it also had a T-O-R multi-structure with a large  $d_{33}$  (630 pC/N). A planar-type actuator was produced using this thick film, and this actuator exhibited a large acceleration (335 G at 120 V/mm) and displacement (231 μm at 120 V/mm). Hence, the KNNS-0.01SZ-0.03BAZ thick film is a good candidate for lead-free piezoelectric actuators.

## 1. Introduction

Lead zirconium titanate (PZT)-based piezoceramics have been utilized in various electronic devices [1–4]. However, they are harmful to human health and the environment because they contain more than 60 wt% PbO. Thus, many efforts have been made to develop lead-free piezoceramics as a substitute for PZT-based piezoceramics [5–7]. (K<sub>1-x</sub>Na<sub>x</sub>)NbO<sub>3</sub>- (KNN)-related lead-free piezoceramics have attracted much attention as substitutions for PZT-based piezoceramics because they exhibit promising piezoelectricity [8–10]. However, the piezoelectricity of KNN-based piezoceramics is still lower than that of PZT-based piezoceramics. Therefore, various techniques have been applied to further improve the piezoelectricity of KNN-based piezoceramics. The reactive template grain growth (RTGG) technique is an effective method for increasing the piezoelectricity of KNN-based piezoceramics [5, 11–14]. NaNbO<sub>3</sub> templates have been employed to texture the grains of the KNN-related piezoceramics along the [001] direction, and their piezoelectric charge constant ( $d_{33}$ ) was found to be significantly improved [5, 13, 14]. Previously, a large  $d_{33}$  (700 pC/N) was obtained from the [001]-oriented (K, Na)(Nb, Sb)O<sub>3</sub>-(Bi, K)HfO<sub>3</sub>-CaZrO<sub>3</sub> piezoceramic [14]. In the RTGG method, however, single-crystal templates have to be used, and the tape casting process should be employed. Therefore, the RTGG process for KNN-based ceramics is complicated compared with the traditional solid-state method.

Synthesis of KNN-based piezoceramics with a multi-structure, in which its constituent structures coexist, is another method to enhance the piezoelectricity of KNN-related piezoceramics. A multi-structure has been developed by transferring the orthorhombic-rhombohedral (O-R) phase transition temperature ( $T_{O-R}$ ) and the tetragonal-orthorhombic (T-O) phase transition temperature ( $T_{T-O}$ ) to room temperature (RT) [15–18]. Various structures, such as O-R, T-O, rhombohedral-tetragonal (R-T), and T-O-R multi-structures, have been synthesized by transferring the  $T_{O-R}$  and  $T_{T-O}$  to RT [9, 19–26]. Pseudocubic-orthorhombic (PC-O) and PC-T multi-structures have also been developed in KNN-based piezoceramics by decreasing the Curie temperature ( $T_C$ ) and  $T_{T-O}$  to near RT [27–31]. KNN-based piezoceramics with the O-R multi-structure show relatively low  $d_{33}$  values (190–230 pC/N) [19–21]. However, KNN-based piezoceramics with other multi-structures exhibit a comparatively large  $d_{33}$  value (418–570 pC/N) [9, 22–26]. Furthermore, KNN-based piezoceramics with nanodomains have been reported to have a large  $d_{33}$  value because the domain boundary energy of the nanodomains is low, resulting in easy domain rotation with high piezoelectricity [32, 33]. The nanodomains were generally observed in KNN-based piezoceramics with relaxor properties [34–36]. In particular, KNN-based piezoceramics that have a T-O-R multi-structure and nanodomains exhibited a large  $d_{33}$  (650 ± 20 pC/N) [36]. Because KNN-related piezoceramics with a multi-structure and nanodomains can be easily synthesized using the traditional solid-state sintering method, the formation of a multi-structure with nanodomains is an easy and convenient technique to enhance the piezoelectric properties of KNN-related piezoceramics.

Various ABO<sub>3</sub>-type additives (A = Ca/Sr/Ba, B = Ti/Zr) have been employed to develop such a structure [16, 27, 29, 37–42]. (Bi<sub>0.5</sub>M<sub>0.5</sub>)NO<sub>3</sub> (M = K/Na/Ag, N = Hf/Zr) additives have also been utilized to form various multi-structures with nanodomains [34, 36, 43–47]. Li<sup>+</sup> and Sb<sup>5+</sup> ions have also been used to develop such a multi-structure by transferring  $T_{O-R}$  and  $T_{T-O}$  to RT [18, 48–50]. Furthermore, the (Bi, Ag)ZrO<sub>3</sub> (BAZ) compound was also utilized to improve the piezoelectricity of KNN-related piezoceramics through the development of a multi-structure with nanodomains, and KNN-based piezoceramics with T-O-R, O-R, R-T, and T-O multi-structures were produced using the BAZ compound; they showed comparatively large  $d_{33}$  values of 235–490 pC/N [47, 51–53]. Moreover, relaxor properties with nanodomains were also observed in the BAZ-added KNN-based piezoceramics. Hence, BAZ is considered to be a promising compound for enhancing the piezoelectric properties of KNN-related piezoceramics through the formation of the multi-structure and nanodomains. In addition, although many KNN-based piezoceramics have been exploited, piezoelectric devices produced by lead-free piezoceramics have rarely been reported. It is thus important to evaluate the applicability of lead-free piezoceramics through the fabrication of piezoelectric devices with good electrical properties.

In this study, therefore, 0.96(K<sub>0.5</sub>Na<sub>0.5</sub>)(Nb<sub>0.93</sub>Sb<sub>0.07</sub>)O<sub>3</sub>-(0.04-x)SrZrO<sub>3</sub>-xBAZ [KNNS-(0.04-x)SZ-xBAZ] piezoceramics were synthesized and their piezoelectric characteristics were studied. The structural properties of these samples were investigated in detail to identify the relationship between the structural properties and piezoelectricity of these samples. In particular, the piezoceramic (x = 0.03) displayed a large  $d_{33}$  (650 pC/N), which was attributed to the existence of the ideal T-O-R multi-structure with nanodomains. Moreover, planar-type actuators were fabricated using KNNS-0.01SZ-0.03BAZ thick films to demonstrate their applicability to piezoelectric devices. This actuator shows excellent actuating properties, confirming that the KNNS-0.01SZ-0.03BAZ piezoceramic developed in this study is a promising lead-free piezoelectric material.

## 2. Experimental Procedures

KNNS-(0.04-x)SZ-xBAZ piezoceramics ( $0.0 \leq x \leq 0.04$ ) were produced using the traditional solid-state method.  $K_2CO_3$ ,  $Na_2CO_3$ ,  $Nb_2O_5$ ,  $Sb_2O_3$ ,  $SrCO_3$ ,  $ZrO_2$ ,  $Bi_2O_3$ , and  $Ag_2O$  (>99%, High Purity Chemicals, Saitama, Japan) powders with the appropriate compositions were ball-milled in Nalgene bottles using yttria-stabilized zirconia balls and anhydrous ethanol for 24 h. Then, 0.5 mol%  $Fe_2O_3$  (>95%, Kanto Chemical, Japan) was added to assist the densification of the samples. After drying, the milled powders were calcined at 850°C for 6 h. The calcined powders were ball-milled again for 24 h and then dried. After granulating the milled powders, disc-shaped pellets were produced by applying a uniaxial pressure of 50 MPa and sintering at 1090°C – 1100°C for 3 h in air.

The calcined KNNS-0.01SZ-0.03BAZ powder ( $x = 0.03$ ) was used to fabricate thick films through the tape-casting process. The calcined KNNS-0.01SZ-0.03BAZ powders, a dispersant, anhydrous ethanol, and toluene were ball-milled for 12 h, and plasticizer and binder were supplied during the second ball-milling process, which was conducted for 36 h. These slurries were utilized to fabricate KNNS-0.01SZ-0.03BAZ green sheets by the tape casting method, after which the green sheets were dried at 65°C. The dried green sheets were cut, stacked, screen-printed, and warm isostatically pressed under 30 MPa at 70°C for 20 min. These sheets were heated to 550°C at 0.2°C/min and maintained for 5 h to eliminate the organics. They were then re-pressed under 200 MPa using a cold isostatic press and were densified at 1090°C–1110°C for various sintering times. The piezoelectric, structural, dielectric, and ferroelectric properties of the KNNS-(0.04-x)SZ-xBAZ piezoceramics ( $0.0 \leq x \leq 0.04$ ) and the KNNS-0.01SZ-0.03BAZ thick films were measured as described in Supporting Information 1.

A KNNS-0.01SZ-0.03BAZ thick film with dimensions of 20 mm × 20 mm × 0.3 mm was affixed to an SUS304 panel using DP-420 epoxy to fabricate a planar-type actuator. A laser Doppler vibrometer (LDV, Polytec, PSV-400, OFV-5000) was used to measure the actuating characteristics of this planar-type actuator, including the vibration acceleration and displacement under a sine wave input voltage. These values were obtained at different frequencies and voltages. The resonance frequencies of the actuators were measured at different voltages. COMSOL software was used to simulate the actuating characteristics, and the experimental values were evaluated using the simulated values.

## 3. Results And Discussion

### 3.1 Piezoelectric properties

The relative densities,  $\varepsilon_{33}^T/\varepsilon_0$ ,  $\tan \delta$ ,  $d_{33}$ , and  $k_p$  values of the KNNS-(0.04-x)SZ-xBAZ piezoceramics ( $0.0 \leq x \leq 0.04$ ) are shown in Fig. 1(a), and these samples were sintered at 1090°C–1100°C for 3 h. All the samples have comparatively large relative densities ( $\geq 94.5\%$  of the theoretical density). Hence, all the specimens were well densified. The  $\varepsilon_{33}^T/\varepsilon_0$  of the piezoceramic ( $x = 0.0$ ) was approximately 1864, and its variation was not significant when  $x$  was less than 0.03. However, a very large  $\varepsilon_{33}^T/\varepsilon_0$  of approximately 3836 was observed for the sample ( $x = 0.03$ ) because the  $T_{T-O-R}$  was developed at approximately RT for this sample, which will be discussed later. The sample ( $x = 0.04$ ) exhibited similar results. The  $\tan \delta$  of the sample ( $x = 0.0$ ) was approximately 4.5%, and it slightly decreased with an increase in  $x$ . The  $d_{33}$  of the piezoceramic ( $x = 0.0$ ) was 360 pC/N and increased with increasing  $x$ , and the largest  $d_{33}$  of 650 pC/N was observed in the piezoceramic ( $x = 0.03$ ). However, it decreased to 523 pC/N for the specimen ( $x = 0.04$ ). Figure 1(b) shows the  $d_{33}$  values for KNN-related lead-free ceramics that have been reported in the literature. The largest  $d_{33}$  value of  $650 \pm 20$  pC/N was observed in the (K, Na)(Nb, Sb)O<sub>3</sub>-(Bi, Na, K)ZrO<sub>3</sub>-Fe<sub>2</sub>O<sub>3</sub>-AgSbO<sub>3</sub> piezoceramics [36]. Therefore, the  $d_{33}$  value observed from the sample ( $x = 0.03$ ) is almost the same as the largest  $d_{33}$  value reported in the literature. The  $k_p$  of the sample ( $x = 0.0$ ) was approximately 0.44, which increased with increasing  $x$ , and the largest  $k_p$  of 0.52 was observed from the sample ( $x = 0.02$ ). The sample ( $x = 0.03$ ) exhibited a similar  $k_p$  of 0.51. The  $k_p$  value is proportional to  $d_{ij}^2/\varepsilon_{33}^T$ . Therefore, the large  $k_p$  of the piezoceramic ( $x = 0.02$ ) is ascribed to its small  $\varepsilon_{33}^T$  and relatively large  $d_{33}$ , and the large  $k_p$  of the sample ( $x = 0.03$ ) is attributed to its large  $d_{33}$  value. The  $d_{33}$  of the sample ( $x = 0.03$ ) was measured at various temperatures to investigate the temperature dependence of the piezoelectricity of this sample (Fig. 1(c)). The  $d_{33}$  slightly decreased with an increase in the measuring temperature, but a relatively high  $d_{33}$  (500 pC/N) was observed at 120°C, implying that this sample preserved comparatively high piezoelectricity up to 120°C. Figure 1(d) shows the variation in the  $d_{33}$  value with respect to the poling temperature for the sample with  $x = 0.03$ . The sample poled at 20°C displayed the largest  $d_{33}$  of 650 pC/N, and a similar result was observed for the sample poled at 30°C. However, it decreased when the poling temperature exceeded 30°C. It has been reported that KNN-based specimens show better piezoelectric properties when they are poled near the phase transition temperature because many structures coexist at the phase transition temperature [54–56]. The piezoceramic ( $x = 0.03$ ) exhibited the largest  $d_{33}$  value of 650 pC/N when it was poled at 20°C–30°C because this sample has a  $T_{T-O-R}$  near RT, which will be shown later. In addition, the polarization–electric field ( $P$ – $E$ ) hysteresis curves of these piezoceramics were also measured (Figs. S1(a)–(f)). The piezoceramic ( $x = 0.03$ ) shows a normal  $P$ – $E$  curve and has a comparatively high saturated polarization ( $P_S$ ) of 21.6  $\mu\text{C}/\text{cm}^2$ , a remnant polarization ( $P_r$ ) of 16.3  $\mu\text{C}/\text{cm}^2$ , and a coercive electric field ( $E_c$ ) of 0.65 kV/mm (Fig. S1(d)), indicating that it has good ferroelectric properties. Moreover, other piezoceramics also exhibited similar ferroelectric properties (Fig. S1(f)).

### 3.2 Structural properties

Figures 2(a)–(d) show the SEM images of the thermally etched surface of the KNNS-(0.04-x)SZ-xBAZ piezoceramics ( $0.0 \leq x \leq 0.04$ ). All the samples had a dense microstructure, resulting in a large relative density (Fig. 1(a)). The sample ( $x = 0.0$ ) has a microstructure consisting of two types of grains: large grains with an average grain size of approximately 20  $\mu\text{m}$  and small grains with an average grain size of 1  $\mu\text{m}$ , as shown in the inset of Fig. 2(a). As BAZ was added, the samples began to exhibit large grains without small grains (Figs. 2(b)–(d)), suggesting that the BAZ assisted the grain growth of the samples. Grain size did not change with an increase in BAZ content, and the average grain size of the samples with  $0.01 \leq x \leq 0.04$  was 23–25  $\mu\text{m}$ . SEM images were also obtained from the fractured surfaces of the samples, and they showed similar results (Figs. S2(a)–(e)). It has been generally accepted that samples with large grains exhibit better piezoelectric properties [57–59]. Hence, these results suggest that the addition of BAZ can enhance the piezoelectric characteristics of the samples by increasing their grain size.

The piezoelectric properties of the KNN-based ceramics were considerably influenced by the crystal structure of the samples. Piezoceramics generally exhibit large piezoelectric properties when they have a T-O-R (or R-T) multi-structure. Hence, it is important to clarify the crystal structure of the KNNS-(0.04-x)SZ-xBAZ ceramics with  $0.0 \leq x \leq 0.04$ . According to the XRD patterns, all the samples have a homogeneous perovskite phase, without a secondary phase (Figs. S3(a)–(e)). However, it is not possible to determine the crystal structure of these samples using the normal XRD pattern. Hence, the XRD peaks at  $66.5^\circ$ , which were obtained by the slow-speed scanning method, were deconvoluted using the Voigt function to investigate the crystal structure of the samples ( $0.0 \leq x \leq 0.04$ ), as displayed in Figs. 3(a)–(e). The sample with  $x = 0.0$  shows rhombohedral  $(220)_R$  and  $(2-20)_R$  peaks, strong orthorhombic  $(004)_O$ ,  $(400)_O$ , and  $(222)_O$  peaks, and weak tetragonal  $(202)_T$  and  $(220)_T$  peaks, indicating that this sample has a T-O-R multi-structure. However, the intensity of the orthorhombic peaks was much larger than those of the rhombohedral and tetragonal peaks for the specimen ( $x = 0.0$ ) (Fig. 3(a)). As the amount of BAZ increased, the intensity of the orthorhombic peaks decreased, and that of the tetragonal structure was enhanced, but the variation in the rhombohedral peak intensity was not significant. For the samples ( $0.0 \leq x \leq 0.02$ ), however, the proportion of the orthorhombic structure was still larger than those of other structures (Figs. 3(a)–(c)). However, each structure had a similar proportion in the sample ( $x = 0.03$ ), as illustrated in Fig. 3(d). Moreover, it can be suggested that this sample has an ideal T-O-R multi-structure because the rhombohedral, orthorhombic, and tetragonal structures have similar proportions. Finally, the sample ( $x = 0.04$ ) exhibited an R-T multi-structure, with a large proportion of the tetragonal structure (Fig. 3(e)).

Rietveld refinement was also performed to determine the detailed crystal structure of the piezoceramic ( $x = 0.03$ ). Various models were used for the Rietveld analysis (Figs. 4(a)–(c)): O-R multi-structure, T-O multi-structure, and T-O-R multi-structure. Table 1 shows the atomic coordinates, site occupancies,  $R$ -values, and lattice parameters of these models. The T-O-R multi-structure that consists of 31%  $R3m$  rhombohedral, 33%  $Amm2$  orthorhombic, and 36%  $P4mm$  tetragonal structures shows the lowest  $R$ -value, as shown in Fig. 4(c). The samples with  $x = 0.0, 0.01$ , and  $0.02$  also have a T-O-R multi-structure, but the amount of orthorhombic structure is larger than those of the other structures, as shown in Figs. S4(a)–(e). Therefore, Rietveld analysis confirmed that the piezoceramic ( $x = 0.03$ ) has an ideal T-O-R multi-structure, in which the three structures have similar proportions. Moreover, it can be suggested that the presence of an ideal T-O-R multi-structure can contribute to the large  $d_{33}$  value of this sample. In addition, the piezoceramic ( $x = 0.04$ ) has an R-T multi-structure, as shown in Figs. S5(a) and (b), which is identical to the R-T morphotropic phase boundary structure of PZT-based piezoceramics. Hence, this piezoceramic also has a comparatively large  $d_{33}$  of 523 pC/N.

Table 1

Atomic coordinates, site occupancies, lattice parameters, and  $R$ -values of the KNNS-0.01SZ-0.03BAZ piezoceramic for O-R, T-O, and T-O-R multi-structure models.

Phase	Structural model (SG)	Site label	x	y	z	Site occupancy	Lattice parameter (Å)	R factor
O-R multi-structure	Orthorhombic (Amm2) (69%)	K/Na/Sr	0(-)	0(-)	0(-)	0.114(-)/0.123(-)/0.002(-)	a = 3.9894(2)	$R_p/R_{wp}/R_{exp}$
		/Bi/Ag				/0.004(-)/0.004(-)	b = 5.6153(3)	$R_b/R_f$
	+ Rhombohedral (R3m, H) (31%)	Nb/Sb/Zr	0.5(-)	0(-)	0.5250(37)	0.224(-)/0.016(-)/0.010(-)	c = 5.6223(3)	4.70 / 6.09 / 3.00
		O1	0(-)	0(-)	0.5205(94)	0.250(-)	$\alpha = \beta = \gamma = 90^\circ$	5.49 / 2.80
		O2	0.5(-)	0.2249(67)	-0.2105(84)	0.500(-)		
		K/Na/Sr	0(-)	0(-)	0.4742(57)	0.076(-)/0.082(-)/0.002(-)	a = b = 5.6289(18)	$R_p/R_{wp}/R_{exp}$
		/Bi/Ag				/0.004(-)/0.002(-)	c = 6.8957(42)	$R_b/R_f$
		Nb/Sb/Zr	0(-)	0(-)	0(-)	0.150(-)/0.010(-)/0.007(-)	$\alpha = \beta = 90^\circ$	4.70 / 6.09 / 3.00
O1	0.5057(-)	-0.5057(-)	0.4805(51)	0.500(-)	$\gamma = 120^\circ$	5.48 / 3.36		
T-O multi-structure	Tetragonal (P4mm) (44%)	K/Na/Sr	0(-)	0(-)	-0.0483(31)	0.057(-)/0.062(-)/0.001(-)	a = 3.9768(1)	$R_p/R_{wp}/R_{exp}$
		/Bi/Ag				/0.002(-)/0.002(-)	c = 3.9801(1)	$R_b/R_f$
	+ Orthorhombic (Amm2) (56%)	Nb/Sb/Zr	0.5(-)	0.5(-)	0.5(-)	0.112(-)/0.008(-)/0.005(-)	$\alpha = \beta = \gamma = 90^\circ$	4.26 / 5.76 / 3.01
		O1	0.5(-)	0.5(-)	0.0155(55)	0.125(-)		4.06 / 2.86
		O2	0.5(-)	0(-)	0.4476(63)	0.250(-)		
		K/Na/Sr	0(-)	0(-)	0(-)	0.114(-)/0.123(-)/0.002(-)	a = 3.9932(2)	$R_p/R_{wp}/R_{exp}$
		/Bi/Ag				/0.004(-)/0.004(-)	b = 5.6134(2)	$R_b/R_f$
		Nb/Sb/Zr	0.5(-)	0(-)	0.4686(58)	0.224(-)/0.016(-)/0.010(-)	c = 5.6176(2)	4.26 / 5.76 / 3.01
O1	0(-)	0(-)	0.4829(199)	0.250(-)	$\alpha = \beta = \gamma = 90^\circ$	3.75 / 2.62		
O2	0.5(-)	0.2499(88)	0.1981(89)	0.500(-)				
T-O-R structure	Tetragonal (P4mm) (36%)	K/Na/Sr	0(-)	0(-)	-0.0680(117)	0.057(-)/0.062(-)/0.001(-)	a = 3.9772(1)	$R_p/R_{wp}/R_{exp}$
		/Bi/Ag				/0.002(-)/0.002(-)	c = 3.9805(1)	$R_b/R_f$
	+ Orthorhombic (Amm2) (33%)	Nb/Sb/Zr	0.5(-)	0.5(-)	0.5(-)	0.112(-)/0.008(-)/0.005(-)	$\alpha = \beta = \gamma = 90^\circ$	4.06 / 5.38 / 3.00
		O1	0.5(-)	0.5(-)	0.0218(63)	0.125(-)		2.75 / 2.06
		O2	0.5(-)	0(-)	0.4741(69)	0.250(-)		
		K/Na/Sr	0(-)	0(-)	0(-)	0.114(-)/0.123(-)/0.002(-)	a = 3.9948(2)	$R_p/R_{wp}/R_{exp}$
	+ Rhombohedral (R3m, H) (31%)	/Bi/Ag				/0.004(-)/0.004(-)	b = 5.6147(2)	$R_b/R_f$
		Nb/Sb/Zr	0.5(-)	0(-)	0.5094(29)	0.224(-)/0.016(-)/0.010(-)	c = 5.6189(2)	4.06 / 5.38 / 3.00
		O1	0(-)	0(-)	0.5724(-)	0.250(-)	$\alpha = \beta = \gamma = 90^\circ$	3.13 / 2.85
		O2	0.5(-)	0.2011(130)	0.2585(-)	0.500(-)		
K/Na/Sr		0(-)	0(-)	0.4467(27)	0.076(-)/0.082(-)/0.002(-)	a = b = 5.6339(11)	$R_p/R_{wp}/R_{exp}$	
/Bi/Ag					/0.002(-)/0.002(-)	c = 6.8980(25)	$R_b/R_f$	
Nb/Sb/Zr	0(-)	0(-)	0(-)	0.150(-)/0.010(-)/0.007(-)	$\alpha = \beta = 90^\circ$	4.06 / 5.38 / 3.00		
O	-0.5109(-)	-0.5109(-)	0.4841(-)	0.500(-)	$\gamma = 120^\circ$	3.06 / 2.51		

### 3.3 Temperature dependence of dielectric properties and domain structure

Figures 5(a)–(e) show the  $\varepsilon_{33}^T/\varepsilon_0$  versus temperature plots for the KNNS-(0.04-x)SZ-xBAZ ceramics with  $0.0 \leq x \leq 0.04$ , ranging between  $-60^\circ\text{C}$  and  $90^\circ\text{C}$ . Variations in the  $T_{T-O}$  and  $T_{O-R}$  peaks are shown in these figures. For the sample ( $x = 0.0$ ), the  $T_{T-O}$  and  $T_{O-R}$  are approximately  $70^\circ\text{C}$  and  $0.0^\circ\text{C}$ , respectively, as shown in Fig. 5(a). The  $T_{T-O}$  decreases and the  $T_{O-R}$  increases with an increase in  $x$ , and they meet at approximately  $25^\circ\text{C}$  for the sample with  $x = 0.03$ , resulting in the formation of  $T_{T-O-R}$  at RT. When  $x$  exceeded 0.03, the orthorhombic phase disappeared and a broad  $T_{R-T}$  was formed at approximately  $10^\circ\text{C}$  for the sample with  $x = 0.04$ . Therefore, the results of the  $\varepsilon_{33}^T/\varepsilon_0$  versus temperature curves are similar to those of the XRD analysis. In addition, the inset of each figure also shows the  $\varepsilon_{33}^T/\varepsilon_0$  versus temperature curve of the corresponding sample that includes  $T_C$ . The  $T_C$  of the sample ( $x = 0.0$ ) was approximately  $154^\circ\text{C}$ , and it increased with an increase in  $x$  to  $185^\circ\text{C}$  for the sample ( $x = 0.04$ ). In particular, the  $T_C$  of the sample ( $x = 0.03$ ) was comparatively high at  $182^\circ\text{C}$ . Therefore, this sample can maintain a high  $d_{33}$  value of up to  $120^\circ\text{C}$ .

The  $\varepsilon_{33}^T/\varepsilon_0$  values of the KNNS-(0.04-x)SZ-xBAZ piezoceramics ( $0.0 \leq x \leq 0.04$ ) were measured at different frequencies to investigate the relaxor properties of these samples. Relaxor ceramics generally have nanodomains with a small domain boundary energy [32–34]. Hence, relaxor piezoceramics with nanodomains have been reported to exhibit high piezoelectric characteristics [32–34]. Figure 6(a) shows the  $\varepsilon_{33}^T/\varepsilon_0$  values measured at various frequencies for the sample ( $x = 0.0$ ). A change in  $T_{T-O}$  was not observed with an increase in frequency, implying that this sample is a normal ferroelectric ceramic. For the sample ( $x = 0.03$ ), however, the  $T_{T-O-R}$  was enhanced with an increase in the measuring frequency, as shown in Fig. 6(b). The temperature difference ( $\Delta T$ ) between the  $T_{T-O-R}$  measured at the lowest frequency and the  $T_{T-O-R}$  measured at the highest frequency was approximately  $11.3^\circ\text{C}$  for the sample with  $x = 0.03$ . Therefore, the sample with  $x = 0.03$  is considered to be a relaxor ceramic, and this ceramic is expected to have ferroelectric nanodomains. The  $\varepsilon_{33}^T/\varepsilon_0$  values were also measured at various frequencies for the samples ( $x = 0.01, 0.02, \text{ and } 0.04$ ), as shown in Figs. S6(a)–(c). The  $\Delta T$  value of the specimen ( $x = 0.01$ ) was  $4.5^\circ\text{C}$ , and it increased with the increase in  $x$ . Therefore, it is considered that the samples with  $x = 0.01, 0.02, \text{ and } 0.04$  also exhibit relaxor characteristics. TEM analysis was performed on the piezoceramics ( $x = 0.0, 0.03$ ) to investigate the domain structure of these samples. Figure 6(c) shows the TEM bright-field image for the sample with  $x = 0.0$ . The domain size of this sample was approximately  $50 \text{ nm} \times 400 \text{ nm}$ , indicating that this sample had relatively large domains. A TEM bright-field image was also observed from the piezoceramic ( $x = 0.03$ ), as shown in Fig. 6(d). Nanodomains with a size of  $2 \text{ nm} \times 15 \text{ nm}$  were formed in this sample, possibly because this sample showed relaxor properties. This result suggests that the presence of ferroelectric nanodomains also contributes to the large  $d_{33}$  value of this sample.

### 3.4 planar-type actuator

A KNNS-0.01SZ-0.03BAZ thick film ( $x = 0.03$ ) with dimensions of  $20 \text{ mm} \times 20 \text{ mm} \times 0.3 \text{ mm}$  was fabricated to produce a planar-type piezoelectric actuator. The crystal structure of this thick film was determined using Rietveld analysis of the XRD pattern, as shown in Fig. 7(a), and was identified as a T-O-R multi-structure consisting of  $R\bar{3}m$  rhombohedral (29.7%),  $Amm2$  orthorhombic (32.9%), and  $P4mm$  tetragonal (37.4 %) structures. Hence, the crystal structure of this thick film was the same as that of the KNNS-0.01SZ-0.03BAZ piezoceramic. The microstructures of the KNNS-0.01SZ-0.03BAZ thick films sintered at various temperatures were also studied. The thick film sintered at  $1080^\circ\text{C}$  shows two types of grains: large and small grains with average grain sizes of  $25 \mu\text{m}$  and  $0.5 \mu\text{m}$ , respectively (Fig. S7(a)). An SEM image of the thick film sintered at  $1090^\circ\text{C}$  is displayed in Fig. 7(b), showing a dense microstructure with large grains with an average grain size of  $25 \mu\text{m}$ , which is similar to the microstructure of the KNNS-0.01SZ-0.03BAZ piezoceramic. The thick films densified at  $1100^\circ\text{C}$  and  $1110^\circ\text{C}$  also displayed an equivalent microstructure (Figs. S7(b) and (c)). Therefore, it can be concluded that the structural properties of the KNNS-0.01SZ-0.03BAZ thick films sintered at temperatures higher than  $1080^\circ\text{C}$  are similar to those of the KNNS-0.01SZ-0.03BAZ piezoceramic.

Figure 7(c) shows the relative densities,  $\varepsilon_{33}^T/\varepsilon_0$ ,  $\tan \delta$ ,  $d_{33}$ , and  $k_p$  values of the KNNS-0.01SZ-0.03BAZ thick films sintered at various temperatures. The thick film sintered at  $1080^\circ\text{C}$  showed a low relative density (90% of the theoretical density), but the thick films sintered at temperatures higher than  $1080^\circ\text{C}$  exhibited a large relative density ( $\geq 93\%$  of the theoretical density). Hence, the KNNS-0.01SZ-0.03BAZ thick film must be densified at temperatures higher than  $1080^\circ\text{C}$ . The  $\varepsilon_{33}^T/\varepsilon_0$  of the thick film sintered at  $1080^\circ\text{C}$  is relatively small at 1666, probably because of its low density, and it increased with increasing sintering temperature to 3390 for the thick film sintered at  $1110^\circ\text{C}$ . The  $\tan \delta$  of the sample sintered at  $1080^\circ\text{C}$  was approximately 3.3%, and it increased slightly with an increase in sintering temperature. The  $d_{33}$  value of the thick film sintered at  $1080^\circ\text{C}$  was low ( $410 \text{ pC/N}$ ), but increased with an increase in the sintering temperature. The thick film sintered at  $1090^\circ\text{C}$  exhibited the largest  $d_{33}$  value,  $630 \text{ pC/N}$ . This  $d_{33}$  value is slightly smaller than that of the KNNS-0.01SZ-0.03BAZ piezoceramic ( $650 \text{ pC/N}$ ), but the difference is not large. The thick films sintered at  $1100^\circ\text{C}$  and  $1110^\circ\text{C}$  exhibited slightly reduced  $d_{33}$  values of  $610 \text{ pC/N}$ . The  $k_p$  value showed an equivalent trend, and a maximum  $k_p$  value of 0.51 was obtained from the thick film densified at  $1090^\circ\text{C}$ . Therefore, the optimum sintering temperature of the KNNS-0.01SZ-0.03BAZ thick film was considered to be  $1090^\circ\text{C}$ . This thick film was also sintered at  $1090^\circ\text{C}$  for various amounts of time; the thick film sintered for 6.0 h showed the best piezoelectric properties (Fig. S7(d)), and this thick film was used to fabricate planar-type piezoelectric actuators.

The planar-type actuator was fabricated using a KNNS-0.01SZ-0.03BAZ thick film with dimensions of  $20 \text{ mm} \times 20 \text{ mm} \times 0.3 \text{ mm}$ , as shown in the schematic diagram in Fig. 8(a). The COMSOL program was used to simulate the actuating characteristics. Figure 8(b) shows a simulated image of

the KNNS-0.01SZ-0.03BAZ planar-type actuator, along with its strain. The accelerations of this actuator were measured at various frequencies and applied voltages, as shown in Fig. 8(c). The maximum accelerations were obtained at 610 Hz, indicating that 610 Hz is the resonance frequency of the actuator. The maximum acceleration increased with an increase in the applied electric field, and a large acceleration of 335 G was obtained under a comparatively small electric field of 120 V/mm (36 V) at 610 Hz. The maximum accelerations, which were measured at various applied voltages and 610 Hz, are displayed in the inset of Fig. 8(c) as black circles. A similar resonance frequency of 620 Hz was obtained from the simulation (Fig. S8(a)). Accelerations of this actuator were calculated at various applied voltages, and the maximum accelerations, which were calculated at the resonance frequency and various applied voltages, are displayed as red circles in the inset of Fig. 8(c). The calculated accelerations are similar to the measured values. Figure 8(d) shows the change in the displacement as a function of the frequency obtained at various applied electric fields for the KNNS-0.01SZ-0.03BAZ planar-type actuator. The maximum displacements were also obtained at 610 Hz and are shown in the inset of Fig. 8(d) as black circles. The displacement increased with an increase in the electric field, as illustrated by the black circles in the inset of Fig. 8(d). The largest displacement of 231  $\mu\text{m}$  was obtained with the application of a low electric field of 120 V/mm. Displacements were also simulated (Fig. S8(b)), and the maximum displacements at different applied voltages are indicated by red circles in the inset of Fig. 8(d). The simulated displacements were also similar to the measured displacements, implying that the experimental results were in good agreement with the calculated results. The PZT-based planar-type haptic actuator with a circular shape showed a large displacement of 427  $\mu\text{m}$  with an applied electric field of 750 V/mm [60], which is almost six times larger than the electric field used in this study. The displacement of the planar-type KNNS-0.01SZ-0.03BAZ actuator can be further enhanced by increasing the applied electric field, indicating that this actuator is capable of generating a larger displacement than the PZT-based planar-type actuator. Therefore, the KNNS-0.01SZ-0.03BAZ lead-free piezoceramic is a promising material for piezoelectric actuators.

## 4. Conclusions

KNNS-(1-x)SZ-xBAZ piezoceramics ( $0.0 \leq x \leq 0.04$ ) were well densified at 1090°C, and they exhibited large relative densities ( $\geq 94.5\%$  of the theoretical density). The  $d_{33}$  value improved with the addition of BAZ, and the largest  $d_{33}$  of 650 pC/N was found for the piezoceramic ( $x = 0.03$ ). This  $d_{33}$  value is equivalent to the largest  $d_{33}$  value of the KNN-related piezoceramics reported in the literature. The large  $d_{33}$  value was maintained up to 120°C, suggesting that this piezoceramic has good thermally stable piezoelectricity. According to the Rietveld analysis, the piezoceramic with  $x = 0.03$  has an ideal T-O-R multi-structure, in which each structure has similar proportions. The sample ( $x = 0.0$ ) is a normal ferroelectric ceramic, but relaxor properties were observed when BAZ was added. Moreover, nanodomains with a size of 2 nm  $\times$  15 nm were found in the sample ( $x = 0.03$ ). Therefore, the piezoceramic ( $x = 0.03$ ) shows a large  $d_{33}$  value of 650 pC/N because of the presence of the ideal T-O-R multi-structure and nanodomains. A KNNS-0.01SZ-0.03BAZ thick film was fabricated to produce a planar-type piezoelectric actuator. This thick film also has a T-O-R multi-structure, large  $d_{33}$  (630 pC/N), and large  $k_p$  (0.51), which are similar to those of the KNNS-0.01SZ-0.03BAZ piezoceramics. The planar-type actuator was fabricated using a KNNS-0.01SZ-0.03BAZ thick film with dimensions of 20 mm  $\times$  20 mm  $\times$  0.2 mm. This actuator showed a large acceleration of 335 G and a displacement of 231  $\mu\text{m}$  at a low electric field of 120 V/mm. Therefore, the KNNS-0.01SZ-0.03BAZ piezoceramic is an excellent material for piezoelectric actuators.

## Declarations

### Acknowledgements

This work was supported by National R&D Programs through the National Research Foundation of Korea (NRF) funded by ICT (Project No. 2020M3H4A3105596). We also thank the KU-KIST Graduate School Program of Korea University.

## References

1. Fialka J, Benes P, Michlovská L, Klusacek S, Pikula S, Dohnal P, Havranek Z (2016) Measurement of thermal depolarization effects in piezoelectric coefficients of soft PZT ceramics via the frequency and direct methods. *J Eur Ceram Soc* 36(11):2727–2738
2. Heywang W, Lubitz K, Wersing W (2008) *Piezoelectricity: Evolution and Future of a Technology*. Springer Science & Business Media, Berlin
3. Sun E, Cao W (2014) Relaxor-based ferroelectric single crystals: Growth, domain engineering, characterization and applications. *Prog Mater Sci* 65:124–210
4. Seo I-T, Lee T-G, Kim D-H, Hur J, Kim J-H, Nahm S, Ryu J, Choi B-Y (2016) Multilayer piezoelectric haptic actuator with CuO-modified PZT-PZNN ceramics. *Sens Actuators A: Phys* 238:71–79
5. Saito Y, Takao H, Tani T, Nonoyama T, Takatori K, Homma T, Nagaya T, Nakamura M (2004) Lead-free piezoceramics. *Nature* 432(7013):84–87
6. Panda P, Sahoo B (2015) PZT to lead free piezo ceramics: A review. *Ferroelectrics* 474(1):128–143
7. Panda P (2009) Environmental friendly lead-free piezoelectric materials. *J Mater Sci* 44(19):5049–5062
8. Li JF, Wang K, Zhu FY, Cheng LQ, Yao FZ (2013) (K, Na) NbO<sub>3</sub>-based lead-free piezoceramics: Fundamental aspects, processing technologies, and remaining challenges. *J Am Ceram Soc* 96(12):3677–3696

9. Zhang Y, Li J-F (2019) Review of chemical modification on potassium sodium niobate lead-free piezoelectrics. *J Mater Chem C* 7(15):4284–4303
10. Zhang N, Zheng T, Wu J (2020) Lead-Free (K, Na) NbO<sub>3</sub>-based materials: Preparation techniques and piezoelectricity. *ACS Omega* 5(7):3099–3107
11. Moriana AD, Zhang S (2018) Lead-free textured piezoceramics using tape casting: A review. *J Materiomics* 4(4):277–303
12. Messing GL, Trolier-McKinstry S, Sabolsky E, Duran C, Kwon S, Brahmaraout B, Park P, Yilmaz H, Rehrig P, Eitel K (2004) Templated grain growth of textured piezoelectric ceramics. *Crit Rev Sol State Mater Sci* 29(2):45–96
13. Gao L, Dursun S, Gurdal AE, Hennig E, Zhang S, Randall CA (2019) Atmospheric controlled processing enabling highly textured NKN with enhanced piezoelectric performance. *J Eur Ceram Soc* 39(4):963–972
14. Li P, Zhai J, Shen B, Zhang S, Li X, Zhu F, Zhang X (2018) Ultrahigh piezoelectric properties in textured (K, Na) NbO<sub>3</sub>-based lead-free ceramics. *Adv Mater* 30(8):1705171
15. Trodahl H, Klein N, Damjanovic D, Setter N, Ludbrook B, Rytz D, Kuball M (2008) Raman spectroscopy of (K, Na) NbO<sub>3</sub> and (K, Na)<sub>1-x</sub>Li<sub>x</sub>NbO<sub>3</sub>. *Appl Phys Lett* 93(26):262901
16. Zhang Y, Li L, Shen B, Zhai J (2015) Effect of orthorhombic–tetragonal phase transition on structure and piezoelectric properties of KNN-based lead-free ceramics. *Dalton Trans* 44(17):7797–7802
17. Wu J, Xiao D, Zhu J (2015) Potassium–sodium niobate lead-free piezoelectric materials: Past, present, and future of phase boundaries. *Chem Rev* 115(7):2559–2595
18. Xing J, Zheng T, Wu J, Xiao D, Zhu J (2018) Progress on the doping and phase boundary design of potassium–sodium niobate lead-free ceramics. *J Adv Dielectr* 8(03):1830003
19. Zhang B, Wu J, Wang X, Cheng X, Zhu J, Xiao D (2013) Rhombohedral–orthorhombic phase coexistence and electrical properties of Ta and BaZrO<sub>3</sub> co-modified (K, Na) NbO<sub>3</sub> lead-free ceramics. *Curr Appl Phys* 13(8):1647–1650
20. Xue D, Shi M, Chen Y, Liu K, Chen Z, Jiang X (2017) Piezoelectric and dielectric properties of lead-free 0.96(K<sub>0.48</sub>Na<sub>0.535</sub>)<sub>0.96</sub>Li<sub>0.04</sub>Nb<sub>1-x</sub>Sb<sub>x</sub>O<sub>3</sub>-0.04CaZrO<sub>3</sub> ceramics with rhombohedral–orthorhombic phase boundary. *Ferroelectrics* 514(1):1–8
21. Zuo R, Fu J, Lv D, Liu Y (2010) Antimony tuned rhombohedral-orthorhombic phase transition and enhanced piezoelectric properties in sodium potassium niobate. *J Am Ceram Soc* 93(9):2783–2787
22. Wu W, Chen M, Wu B, Ding Y, Liu C (2017) Lead-free (K, Na)(Nb, Sb)O<sub>3</sub>-Zn<sub>1-x</sub>(Bi<sub>0.5</sub>K<sub>0.5</sub>)<sub>x</sub>ZrO<sub>3</sub> ceramics: Phase evolution and electrical properties. *J Alloy Compd* 695:2981–2986
23. Jiang L, Li Y, Xing J, Wu J, Chen Q, Liu H, Xiao D, Zhu J (2017) Phase structure and enhanced piezoelectric properties in (1-x)(K<sub>0.48</sub>Na<sub>0.52</sub>)(Nb<sub>0.95</sub>Sb<sub>0.05</sub>)O<sub>3</sub>-x(Bi<sub>0.5</sub>Na<sub>0.42</sub>Li<sub>0.08</sub>)<sub>0.9</sub>Sr<sub>0.1</sub>ZrO<sub>3</sub> lead-free piezoelectric ceramics. *Ceram Inter* 43(2):2100–2106
24. Pan D, Guo Y, Fu X, Guo R, Duan H, Chen Y, Li H, Liu H (2017) Composition induced rhombohedral–tetragonal phase boundary and high piezoelectric activity in (K<sub>0.48</sub>, Na<sub>0.52</sub>)(Nb<sub>(1-x)</sub>Sb<sub>x</sub>)O<sub>3</sub>-0.05Ca<sub>0.2</sub>(Bi<sub>0.5</sub>, Na<sub>0.5</sub>)<sub>0.8</sub>ZrO<sub>3</sub> lead-free piezoelectric ceramics. *Sol State Comm* 259:29–33
25. Tao H, Wu W, Wu J (2016) Electrical properties of holmium doped (K, Na)(Nb, Sb)O<sub>3</sub>-(Bi, Na) HfO<sub>3</sub> ceramics with wide sintering and poling temperature range. *J Alloy Compd* 689:759–766
26. Xing J, Tan Z, Jiang L, Chen Q, Wu J, Zhang W, Xiao D, Zhu J (2016) Phase structure and piezoelectric properties of (1-x)K<sub>0.48</sub>Na<sub>0.52</sub>Nb<sub>0.95</sub>Sb<sub>0.05</sub>O<sub>3</sub>-x(Bi<sub>0.5</sub>Na<sub>0.5</sub>)<sub>0.9</sub>(Li<sub>0.5</sub>Ce<sub>0.5</sub>)<sub>0.1</sub>ZrO<sub>3</sub> lead-free piezoelectric ceramics. *J Appl Phys* 119(3):034101
27. Lee KT, Lee TG, Kim SW, Chae SJ, Kim EJ, Kim JS, Choi JW, Nahm S (2019) Thermally stable high strain and piezoelectric characteristics of (Li, Na, K)(Nb, Sb)O<sub>3</sub>-CaZrO<sub>3</sub> ceramics for piezo actuators. *J Am Ceram Soc* 102(10):6115–6125
28. Lee T-G, Nahm S (2019) Review of sintering technologies, structural characteristics, and piezoelectric properties of NKN-based lead-free ceramics. *Trans Electr Electron Mater* 20(5):385–402
29. Lee KT, Kim DH, Park JS, Lee TG, Cho SH, Park SJ, Kang JY, Nahm S (2017) Orthorhombic-pseudocubic phase transition and piezoelectric properties of (Na<sub>0.5</sub>K<sub>0.5</sub>)(Nb<sub>1-x</sub>Sb<sub>x</sub>)-SrZrO<sub>3</sub> ceramics. *J Am Ceram Soc* 100(10):4827–4835
30. Lee K-T, Kim D-H, Cho S-H, Kim J-S, Ryu J, Ahn C-W, Lee T-H, Kim G-H, Nahm S (2019) Pseudocubic-based polymorphic phase boundary structures and their effect on the piezoelectric properties of (Li, Na, K)(Nb, Sb)O<sub>3</sub>-SrZrO<sub>3</sub> lead-free ceramics. *J Alloy Compd* 784:1334–1343
31. Lee T-G, Cho S-H, Kim D-H, Hwang H-G, Lee K-T, Hong C-H, Hong Y-W, Chae KH, Choi J-W, Kim J-S (2019) Various cubic-based polymorphic phase boundary structures in (1-y)(Na<sub>0.5</sub>K<sub>0.5</sub>)(Nb<sub>1-x</sub>Sb<sub>x</sub>)-yCaTiO<sub>3</sub> ceramics and their piezoelectric properties. *J Eur Ceram Soc* 39(4):973–985
32. Manley ME, Abernathy DL, Sahul R, Parshall DE, Lynn JW, Christianson AD, Stonaha PJ, Specht ED, Budai JD (2016) Giant electromechanical coupling of relaxor ferroelectrics controlled by polar nanoregion vibrations. *Sci Adv* 2(9):e1501814
33. Lv X, Zhang X-x, Wu J (2020) Nano-domains in lead-free piezoceramics: A review. *J Mater Chem A* 8(20):10026–10073
34. Zheng T, Wu H, Yuan Y, Lv X, Li Q, Men T, Zhao C, Xiao D, Wu J, Wang K (2017) The structural origin of enhanced piezoelectric performance and stability in lead free ceramics. *Energy Environ Sci* 10(2):528–537

35. Lv X, Zhu J, Xiao D, Zhang X-x, Wu J (2020) Emerging new phase boundary in potassium sodium-niobate based ceramics. *Chem Soc Rev* 49(3):671–707
36. Tao H, Wu H, Liu Y, Zhang Y, Wu J, Li F, Lyu X, Zhao C, Xiao D, Zhu J (2019) Ultrahigh performance in lead-free piezoceramics utilizing a relaxor slush polar state with multiphase coexistence. *J Am Chem Soc* 141(35):13987–13994
37. Cen Z, Huan Y, Feng W, Yu Y, Zhao P, Chen L, Zhu C, Li L, Wang X (2018) A high temperature stable piezoelectric strain of KNN-based ceramics. *J Mater Chem A* 6(41):19967–19973
38. Wu J, Xiao D, Wang Y, Wu W, Zhang B, Li J, Zhu J (2008) CaTiO<sub>3</sub>-modified [(K<sub>0.5</sub>Na<sub>0.5</sub>)<sub>0.94</sub>Li<sub>0.06</sub>](Nb<sub>0.94</sub>Sb<sub>0.06</sub>)O<sub>3</sub> lead-free piezoelectric ceramics with improved temperature stability. *Scripta Mater* 59(7):750–752
39. Wu J, Xiao D, Wang Y, Wu W, Zhang B, Zhu J (2008) CaTiO<sub>3</sub>-modified (K<sub>0.50</sub>Na<sub>0.50</sub>)(Nb<sub>0.96</sub>Sb<sub>0.04</sub>)O<sub>3</sub> lead-free piezoelectric ceramics. *J Am Ceram Soc* 91(10):3402–3404
40. Guo Y, Kakimoto K-i, Ohsato H (2004) Dielectric and piezoelectric properties of lead-free (Na<sub>0.5</sub>K<sub>0.5</sub>)NbO<sub>3</sub>-SrTiO<sub>3</sub> ceramics. *Sol State Comm* 129(5):279–284
41. Luo J, Zhang S, Zhou Z, Zhang Y, Lee HY, Yue Z, Li JF (2019) Phase transition and piezoelectricity of BaZrO<sub>3</sub>-modified (K, Na)NbO<sub>3</sub> lead-free piezoelectric thin films. *J Am Ceram Soc* 102(5):2770–2780
42. Zuo R, Fu J (2011) Rhombohedral-tetragonal phase coexistence and piezoelectric properties of (NaK)(NbSb)O-LiTaO<sub>3</sub>-BaZrO<sub>3</sub> lead-free ceramics. *J Am Ceram Soc* 94(5):1467–1470
43. Lv X, Wu J, Xiao D, Zhu J, Zhang X (2017) Electric field-induced phase transitions and composition-driven nanodomains in rhombohedral-tetragonal potassium-sodium niobate-based ceramics. *Acta Mater* 140:79–86
44. Xu K, Li J, Lv X, Wu J, Zhang X, Xiao D, Zhu J (2016) Superior piezoelectric properties in potassium-sodium niobate lead-free ceramics. *Adv Mater* 28(38):8519–8523
45. Wu B, Wu H, Wu J, Xiao D, Zhu J, Pennycook SJ (2016) Giant piezoelectricity and high Curie temperature in nanostructured alkali niobate lead-free piezoceramics through phase coexistence. *J Am Chem Soc* 138(47):15459–15464
46. Lv X, Wu J, Yang S, Xiao D, Zhu J (2016) Identification of phase boundaries and electrical properties in ternary potassium-sodium niobate-based ceramics. *ACS Appl Mater Interf* 8(29):18943–18953
47. Sun X-x, Zhang J, Lv X, Zhang X-x, Liu Y, Li F, Wu J (2019) Understanding the piezoelectricity of high-performance potassium sodium niobate ceramics from diffused multi-phase coexistence and domain feature. *J Mater Chem A* 7(28):16803–16811
48. Fu Z, Yang J, Lu P, Zhang L, Yao H, Xu F, Li Y (2017) Influence of secondary phase on polymorphic phase transition in Li-doped KNN lead-free ceramics. *Ceram Inter* 43(15):12893–12897
49. Hollenstein E, Damjanovic D, Setter N (2007) Temperature stability of the piezoelectric properties of Li-modified KNN ceramics. *J Eur Ceram Soc* 27(13–15):4093–4097
50. Wang K, Li JF (2010) Domain engineering of lead-free Li-modified (K, Na) NbO<sub>3</sub> polycrystals with highly enhanced piezoelectricity. *Adv Funct Mater* 20(12):1924–1929
51. Lv X, Wu J, Zhang X-x (2020) Reduced degree of phase coexistence in KNN-based ceramics by competing additives. *J Eur Ceram Soc* 40(8):2945–2953
52. Wang X, Wu J, Lv X, Tao H, Cheng X, Zheng T, Zhang B, Xiao D, Zhu J (2014) Phase structure, piezoelectric properties, and stability of new K<sub>0.48</sub>Na<sub>0.52</sub>NbO<sub>3</sub>-Bi<sub>0.5</sub>Ag<sub>0.5</sub>ZrO<sub>3</sub> lead-free ceramics. *J Mater Sci Mater Electron* 25(7):3219–3225
53. Wang X, Wu J, Xiao D, Cheng X, Zheng T, Lou X, Zhang B, Zhu J (2014) New potassium-sodium niobate ceramics with a giant d<sub>33</sub>. *ACS Appl. Mater Interf* 6(9):6177–6180
54. Huan Y, Wang X, Zhang S, Gao R, Li L (2013) Effect of poling temperature on piezoelectric coefficient in (Na<sub>0.52</sub>K<sub>0.4425</sub>Li<sub>0.0375</sub>)(Nb<sub>0.86</sub>Ta<sub>0.06</sub>Sb<sub>0.08</sub>)O<sub>3</sub> ceramics. *Phys Status Solidi (a)* 210(12):2579–2582
55. Tao H, Wang Z, Zhao S, Zhao C, Yin J, Wu J (2020) Poling temperature-insensitive piezoelectric constant of high-performance potassium sodium niobate piezoceramics. *J Am Ceram Soc* 103(8):4402–4410
56. Zheng T, Wu J (2016) Relationship between poling characteristics and phase boundaries of potassium-sodium niobate ceramics. *ACS Appl Mater Interf* 8(14):9242–9246
57. Cen Z, Yu Y, Zhao P, Chen L, Zhu C, Li L, Wang X (2019) Grain configuration effect on the phase transition, piezoelectric strain and temperature stability of KNN-based ceramics. *J Mater Chem C* 7(5):1379–1387
58. Yang W, Li P, Wu S, Li F, Shen B, Zhai J (2019) A study on the relationship between grain size and electrical properties in (K, Na)NbO<sub>3</sub>-based lead-free piezoelectric ceramics. *Adv Electron Mater* 5(12):1900570
59. Jiang L, Xing J, Tan Z, Wu J, Chen Q, Xiao D, Zhu J (2016) High piezoelectricity in (K, Na)(Nb, Sb)O<sub>3</sub>-(Bi, La, Na, Li)ZrO<sub>3</sub> lead-free ceramics. *J Mater Sci* 51(10):4963–4972

Figures

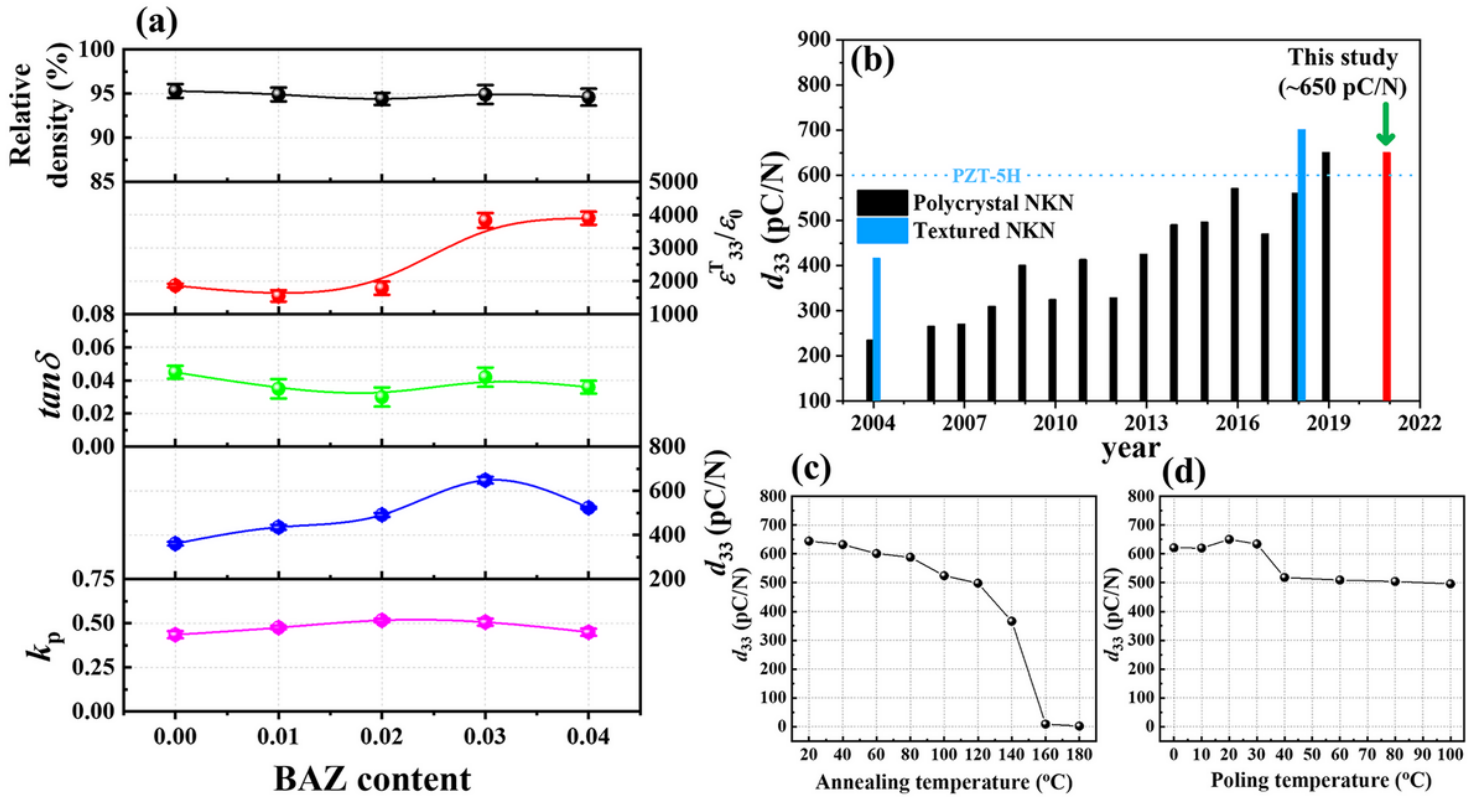


Figure 1 (a) Relative densities and  $\epsilon^T_{33}/\epsilon_0$ ,  $\tan \delta$ ,  $d_{33}$ , and  $k_p$  values of the KNNS-(0.04-x)SZ-xBAZ ceramics ( $0.0 \leq x \leq 0.04$ ). (b)  $d_{33}$  values of KNN-based lead-free piezoceramics reported in the literature. (c)  $d_{33}$  of the piezoceramic ( $x = 0.03$ ) measured at various temperatures. (d) Variation of the  $d_{33}$  value as a function of the poling temperature for the sample with  $x = 0.03$ .

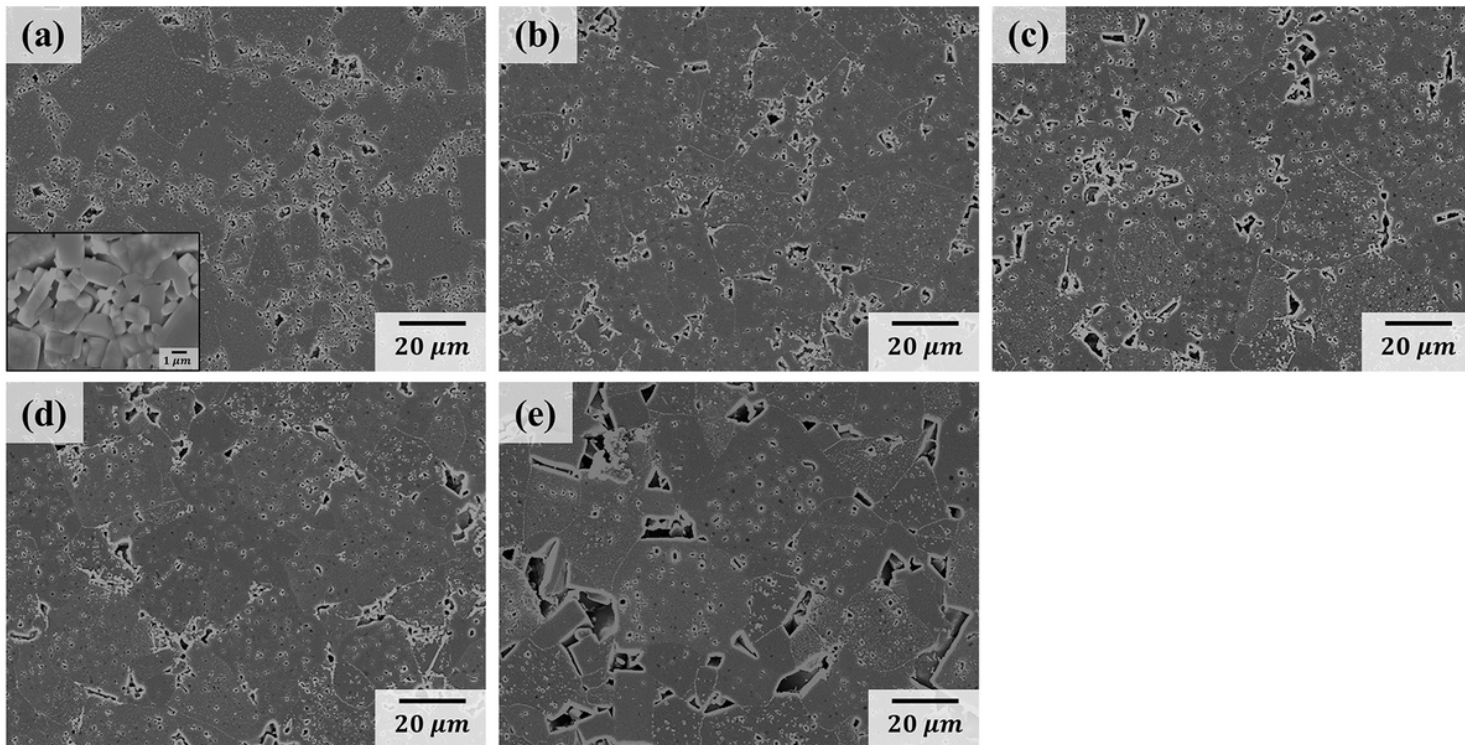


Figure 2

SEM images of the thermally etched surface of KNNS-(0.04-x)SZ-xBAZ piezoceramics with: (a)  $x = 0.0$ , (b)  $x = 0.01$ , (c)  $x = 0.02$ , (d)  $x = 0.03$ , and (e)  $x = 0.04$ .

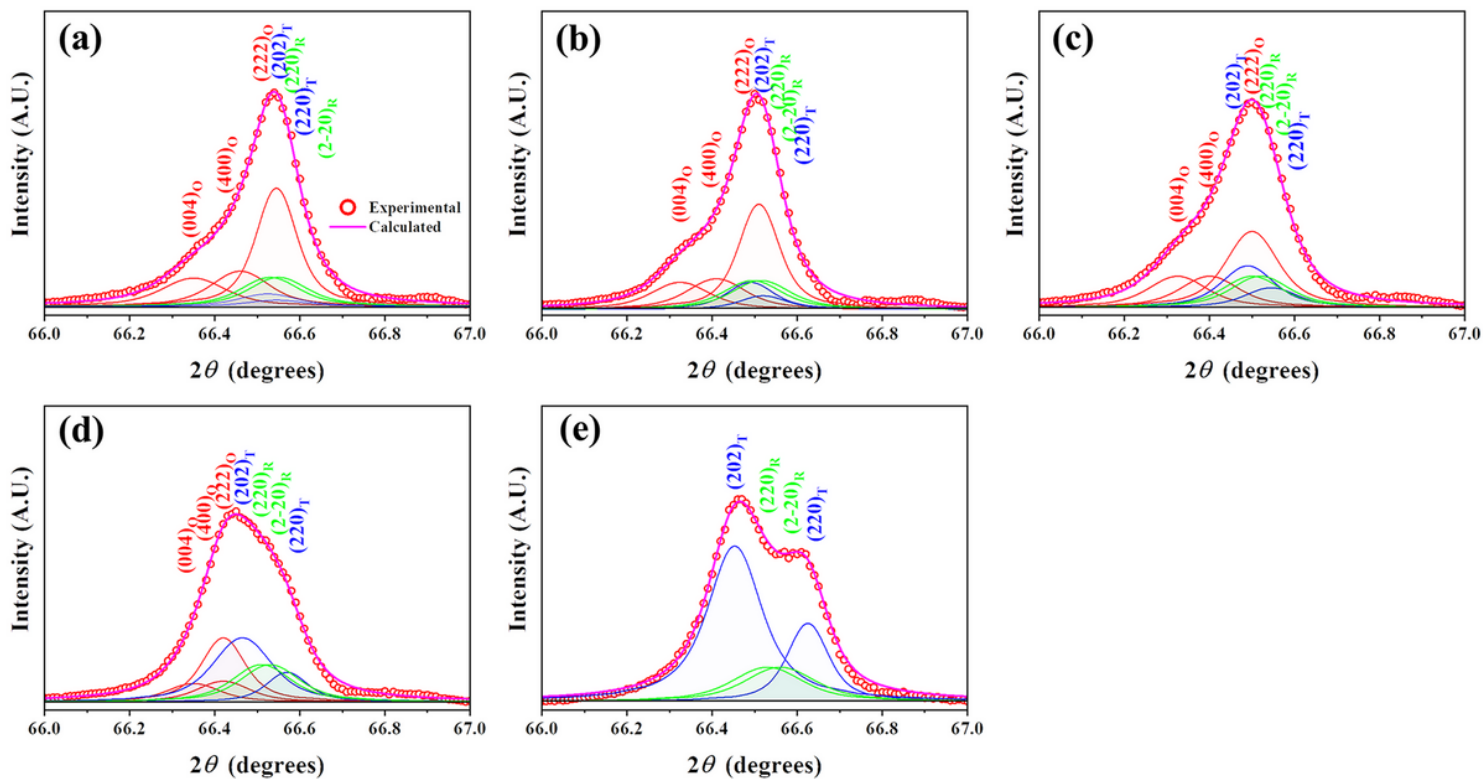


Figure 3

XRD peaks at  $66.5^\circ$  measured by slow-speed scanning and deconvoluted using the Voigt function for the KNNS-(0.04-x)SZ-xBAZ piezoceramics with: (a)  $x = 0.0$ , (b)  $x = 0.01$ , (c)  $x = 0.02$ , (d)  $x = 0.03$ , and (e)  $x = 0.04$ .

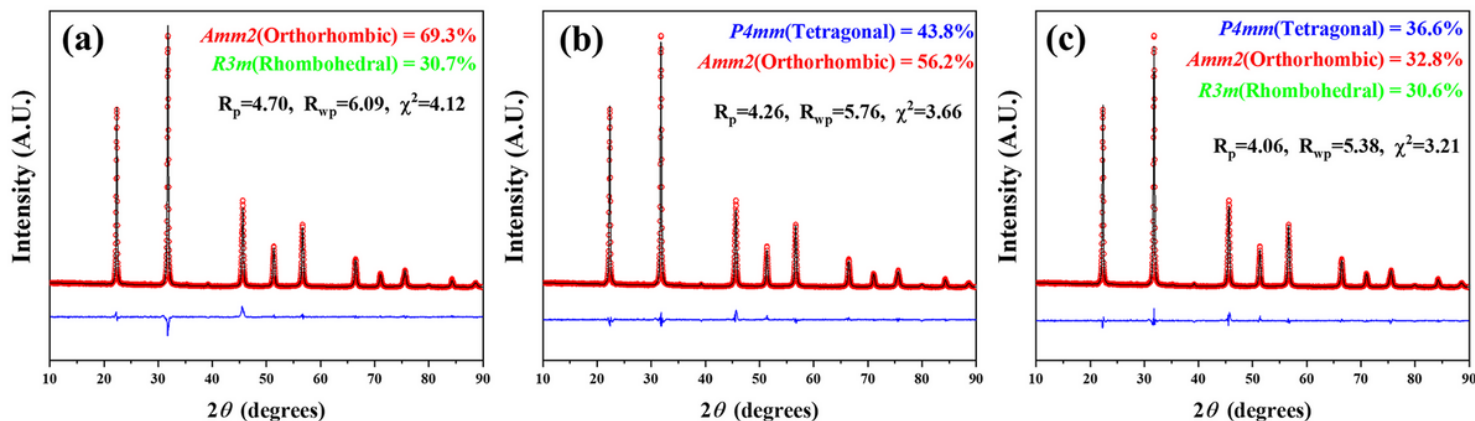


Figure 4

Rietveld refinement of the XRD profiles for the KNNS-0.01SZ-0.03BAZ piezoceramic using the (a) O-R multi-structure, (b) T-O multi-structure, and (c) T-O-R multi-structure.

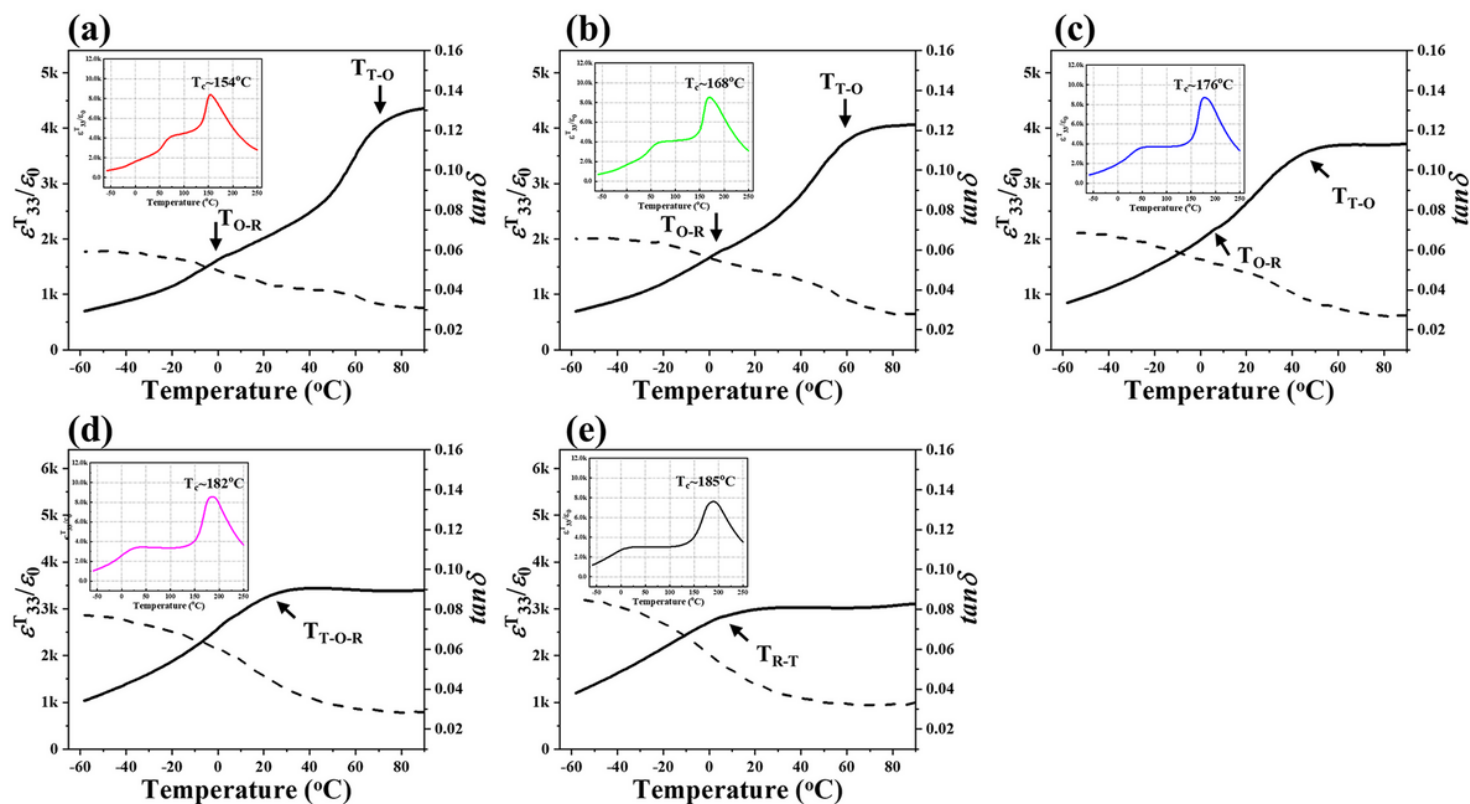


Figure 5

$\epsilon_{T33}/\epsilon_0$  versus temperature curves of the KNNS-(0.04-x)SZ-xBAZ piezoceramics between -60 °C and 90 °C: (a) x = 0.0, (b) x = 0.01, (c) x = 0.02, (d) x = 0.03, and (e) x = 0.04. Inset of each figure displays the  $\epsilon_{T33}/\epsilon_0$  versus temperature curve of the corresponding sample that includes TC.

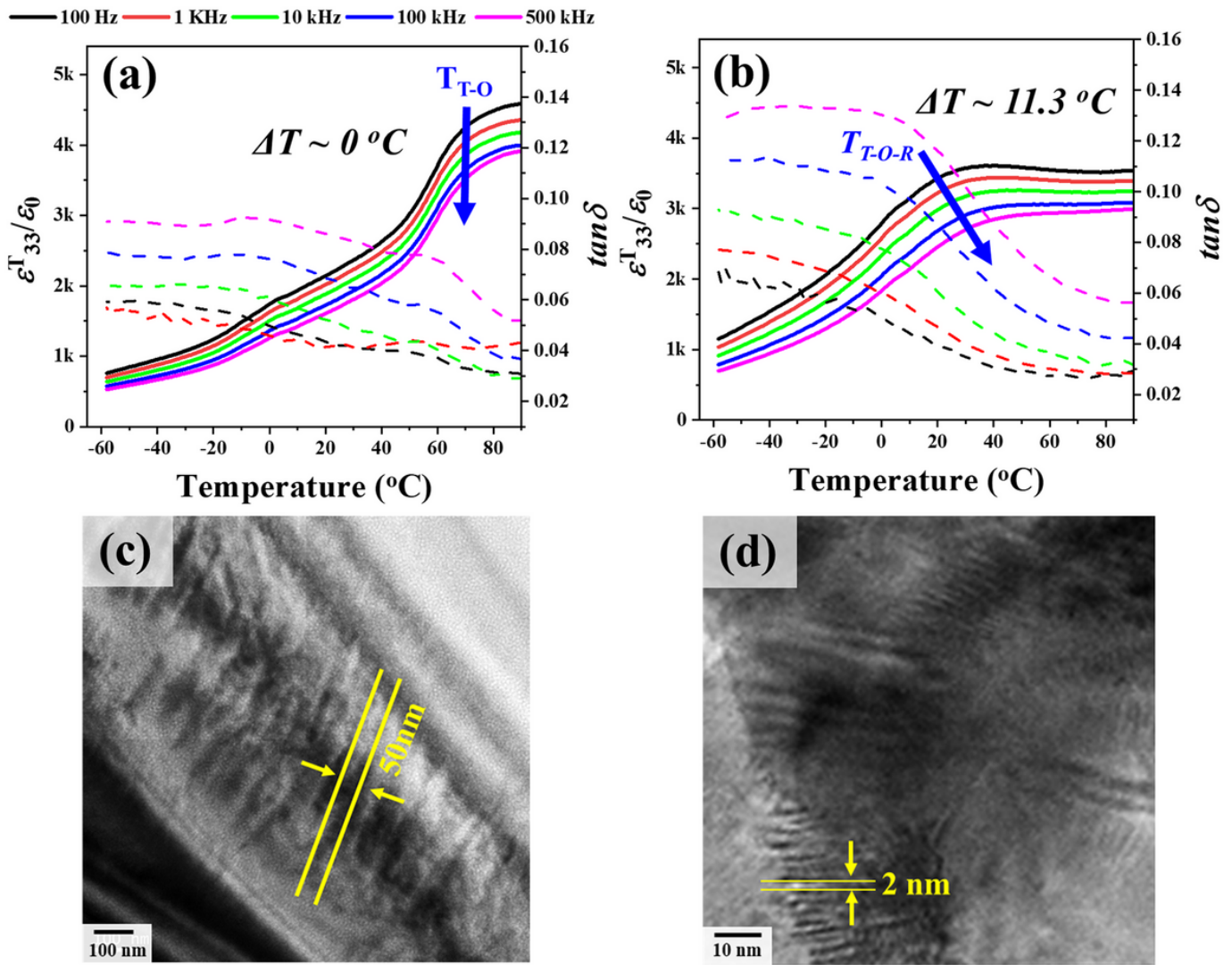


Figure 6

$\epsilon_{33}^T/\epsilon_0$  versus temperature curves obtained at various frequencies for the KNNS-(1-x)SZ-xBAZ piezoceramics with: (a)  $x = 0.0$  and (b)  $x = 0.03$ . TEM bright field images of the KNNS-(0.04-x)SZ-xBAZ piezoceramics with: (c)  $x = 0.0$  and (d)  $x = 0.03$ .

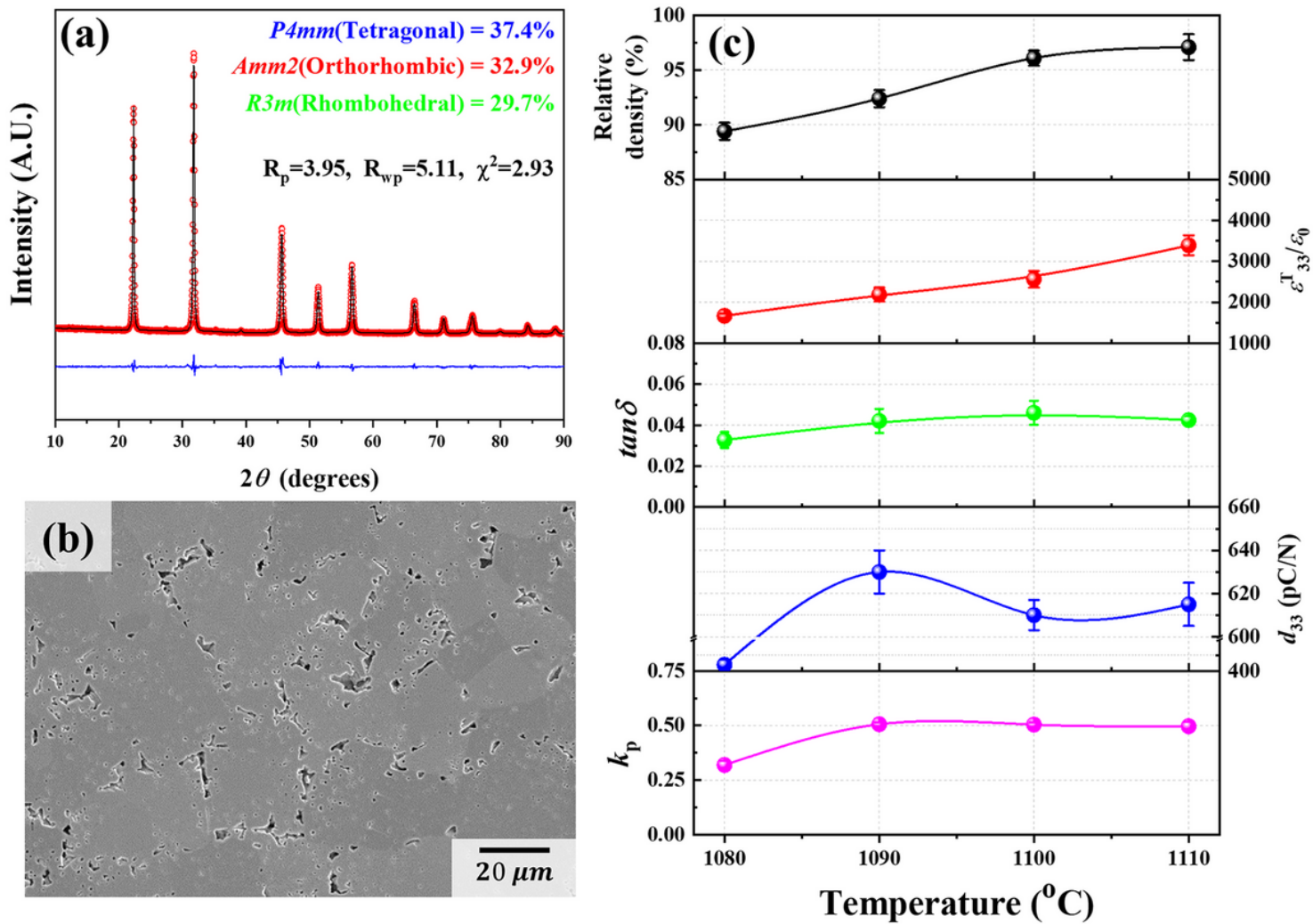


Figure 7

(a) Rietveld refinement of the XRD profile and (b) SEM image of the thermally etched surface for the KNNS-0.01SZ-0.03BAZ thick film. (c) Relative densities and  $\epsilon_{33}^T/\epsilon_0$ ,  $\tan \delta$ ,  $d_{33}$ , and  $k_p$  values of the KNNS-0.01SZ-0.03BAZ thick films sintered at various temperatures.

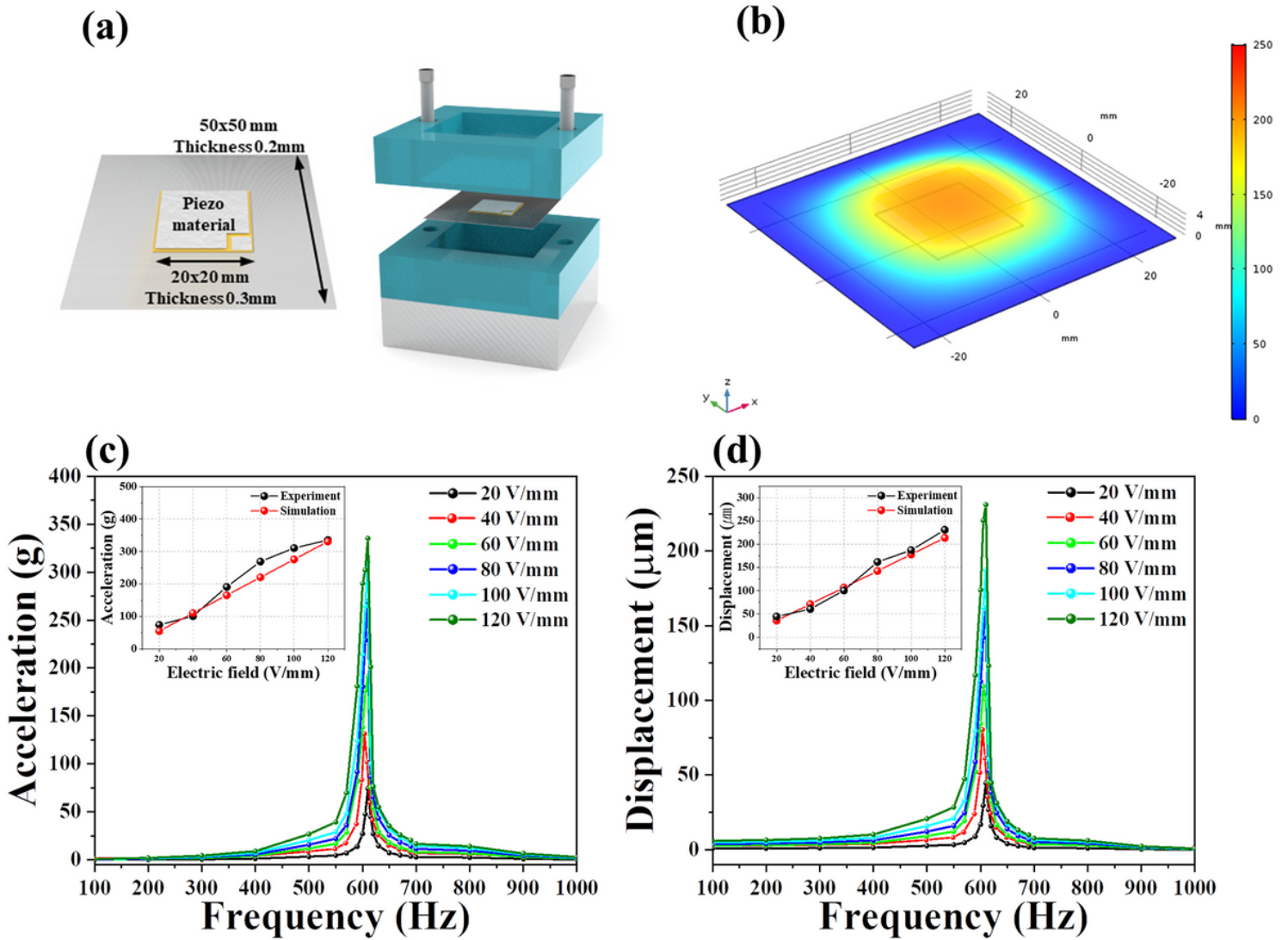


Figure 8

(a) Schematic diagram of the planar-type KNNS-0.01SZ-0.03BAZ actuator and (b) simulated image of the planar-type KNNS-0.01SZ-0.03BAZ actuator. (c) Change in acceleration as a function of the frequency measured at various electric fields for the planar-type KNNS-0.01SZ-0.03BAZ actuator. Inset shows the accelerations measured and calculated at resonance frequency and various applied electric fields. (d) Variation of the displacement as a function of the frequency obtained at various electric fields for the KNNS-0.01SZ-0.03BAZ actuator. Inset shows the displacements measured and calculated at various applied electric fields and resonance frequency.

## Supplementary Files

This is a list of supplementary files associated with this preprint. Click to download.

- [SupplementaryMaterial.docx](#)